Water-retention properties and microstructure changes of a bentonite pellet upon wetting/drying; application to radioactive waste disposal

Agustín Molinero Guerra, Pierre Delage, Yu-Jun Cui, Mokni Nadia, Anh Minh A.M. Tang, Patrick Aimedieu, Frédéric Bernier, Michel Bornert

Water-retention properties and microstructure changes of a bentonite pellet upon wetting/drying; application to radioactive waste disposal

Agustín Molinero-Querra*§, Pierre Delage†, Yu-Jun Cui‡, Nadia Mokni§, Anh Minh Tang‡, Patrick Aimedieu‡, Frédéric Bernier‖ and Michel Bornert‡

Like bricks of compacted bentonite/sand mixtures, mixtures made up of pellets and powder of bentonite are considered as a possible material to make the sealing plugs used to fill up galleries and ensure long-term watertightness in deep radioactive waste disposal. Pellets/bentonite mixtures have a low permeability, high swelling capacity, good radionuclide retention capability and operational advantages in terms of placement in the galleries. Following a previous in-depth characterisation of bentonite pellets/powder mixture conducted by the same group, an investigation of the water-retention properties and microstructure changes of a bentonite pellet subjected to wetting/drying cycles under free swelling conditions was carried out by means of mercury intrusion porosimetry (MIP) and X-ray microtomography. A complete description of the changes in water content, void ratio and degree of saturation of the pellet was provided. Data showed that the free swelling of the pellet is due to the combined effect of both crack propagation at the macro scale, and the swelling of bentonite grains, governed by hydration mechanisms along the smectite faces at the nano scale. Significant development of a crack network is observed between 38 and 9 MPa. For suctions below 9 MPa, there is a significant decrease of the platelet thickness and an increase in the disorder of the platelet assembly, resulting in the average MIP entrance pore radius increasing to 0·4 μm within the expanded bentonite grains.

KEYWORDS: clays; expansive soils; fabric/structure of soils; partial saturation; particle-scale behaviour; radioactive waste disposal

INTRODUCTION

Sealing plugs made of a mixture of bentonite powder/pellets are considered as a possible option to close the galleries excavated for deep geological radioactive waste disposal. Powdered/pelleted bentonite mixtures have low permeability, high swelling capacity and high radionuclide retardation properties. They are also easy to store, transport and install in the galleries and allow for reduced gaps between the host rock and the seal once hydrated. The high density of both the pellets and the powder grains allows a high final dry density of the seal to be obtained once hydrated and, as a result, an adequate swelling pressure. When installed in the gallery, powdered/pelleted bentonite mixtures are initially unsaturated. They are afterwards hydrated under constrained volume owing to the infiltration of pore water from the host rock, which generates a swelling pressure that enables sealing of the gallery by filling all pre-existing inter-grain and inter-pellet voids.

Many investigations have been carried out on the hydro-mechanical behaviour of engineered barriers made up of either compacted pure bentonite or compacted bentonite/sand mixtures in the context of radioactive waste disposal (e.g. Pusch, 1982; Graham *et al.*, 1989; Komine & Ogata, 1994, 1999; Dixon *et al.*, 1996; Alonso *et al.*, 2005; Wang *et al.*, 2013, 2014; Saba *et al.*, 2014; Sun *et al.*, 2014). These investigations have been completed by microstructure investigations carried out using mercury intrusion porosimetry (MIP), scanning electron microscopy (SEM) and environmental SEM (ESEM) (e.g. Montes *et al.*, 2001; Cui *et al.*, 2002; Agus & Schanz, 2005; Delage *et al.*, 2006; Saba *et al.*, 2014; Seiphoori *et al.*, 2014) and X-ray computed microtomography (X-ray μCT) (Kozaki *et al.*, 2001; Kawaragi *et al.*, 2009).

An alternative to the use of engineered barriers made up of bricks of compacted bentonite or sand/bentonite mixtures is that of high-density pellets, or pellets/bentonite powder mixtures. Compared to bricks, the pellets have the advantage of much easier transportation and setting up in the galleries. They also allow for reduced technical voids at interfaces between the canisters or at the top of the gallery. Fig. 1 shows as an example of the concept developed by Nagra, the Swiss agency for the management of radioactive waste, in which the canisters are placed on compacted bricks prior to being surrounded by pellets.

The swelling capacity of pellets has been investigated by various authors, including Imbert & Villar (2006), who performed a series of infiltration tests on a 50/50% FoCa bentonite pellets/powder mixture at different dry densities. (FoCa is a calcium bentonite from the Paris Basin.) They concluded that, once full saturation was reached, the mixture became homogeneous with a swelling pressure equal to that of a bentonite powder compacted at the same dry density. The changes in micro-fabric during hydration of the same mixture at a dry unit weight of 1·36 Mg/m^3 were investigated by Van Geet *et al.* (2005) by using X-ray μCT. They observed a progressive decrease in the density of the pellets during wetting, leading to a final homogenisation of the mixture at complete saturation.

* Formerly Ecole des Ponts ParisTech, Laboratoire Navier/CERMES, Marne La Vallée, France; now Terrasol, Paris, France.
† Ecole des Ponts ParisTech, Laboratoire Navier/CERMES, Marne La Vallée, France (Orcid:0000-0002-2101-5522).
‡ Ecole des Ponts ParisTech, Laboratoire Navier/CERMES, Marne La Vallée, France.
§ Institut de Radioprotection et de Sûreté Nucléaire (IRSN), Fontenay-aux-Roses, France.
‖ Agence Fédérale de Contrôle Nucléaire (AFCN), Brussels, Belgium.

Fig. 1. Nagra concept, based on bentonite blocks and bentonite pellets

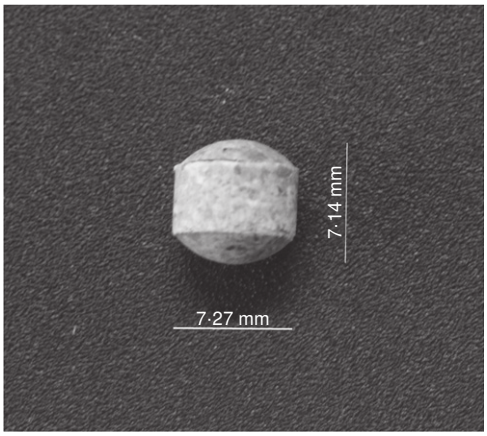

Fig. 2. Pellet at initial state

Few studies have been conducted on the hydro-mechanical behaviour of bentonite pellets. Sugita *et al*. (2005) performed a characterisation of hydraulic, swelling and thermal properties of MX80 bentonite pellets by means of a full-scale experiment called the prototype repository project (PRP), carried out in the Aspoe underground research laboratory (Svemar & Pusch, 2000) in Sweden. The purpose of their study was to validate some assumptions with respect to the numerical simulation of the engineered barrier system (EBS) in the PRP. They concluded that the mass of pellets could be assimilated to a homogeneous high-density block in numerical simulations. Hoffmann *et al*. (2007) characterised the hydro-mechanical behaviour of mixtures of compacted pellets at different dry densities considered within the framework of the EB project (Schuster *et al*., 2014). They determined the pore size distribution of mixtures of pellets of different sizes compacted at different densities, evidencing three main groups of pores – namely, the inter-aggregate, intra-aggregate and inter-pellets pores. The pore size density function of a single pellet was also determined, with two pore populations (intra-aggregate and inter-aggregate pores). Karnland *et al*. (2008) investigated the swelling pressure and hydraulic conductivity of Wyoming bentonite materials under three configurations: granulated material (maximum grain size of approximately 10 mm) without any pre-treatment, granulated material compacted into pellets and a mixture of 70% bentonite and 30% sand. They confirmed the findings of Imbert & Villar (2006) on a 50/50 bentonite powder/pellet mixture – at the same density there is no significant difference after hydration, in terms of final swelling pressure and hydraulic conductivity, between the bentonite pellets and the granulated bentonite material.

Following a previous work in which the initial state of a bentonite pellet was investigated in detail (Molinero-Guerra *et al*., 2016), the aim of the present work is to investigate the water-retention properties and the microstructure changes of a bentonite pellet under wetting/drying paths. The changes in microstructure of samples submitted to various controlled suctions by means of the vapour control technique were investigated by MIP tests carried out on freeze-dried specimens, complemented by X-ray μCT observations.

MATERIALS AND METHODS

Material studied

The pellet is made up of bentonite from Wyoming (USA) with high smectite content (80%) and some inclusions of non-clayey minerals (quartz – 4% of the total mass; muscovite – 4% of the total mass; pyrite – less than 1% of the total mass; and some elements of calcite). The pellets were provided by the Laviosa-MPC company, under the commercial name Expangel SP7, but they are commonly identified by another commercial name, MX80. The cation exchange capacity (CEC) is 98 meq/100 g, with Na^+ as the major exchangeable cation (52 meq/100 g, with also 1·2 meq/100 g for K^+, 10 meq/100 g for Mg^{++} and 37 meq/100 g for Ca^{++}). The liquid limit is 560%, the plastic limit is 62% and the unit mass is 2·77 Mg/m^3 (Saba, 2013).

Pellets were industrially produced by the Laviosa-MPC company by compacting bentonite powder into a mould of 7 mm dia. and 7 mm high. Compaction was performed at a water content of $6 \pm 1\%$ by applying the compaction effort instantaneously, resulting in a pellet dry density $\rho_d = 2{\cdot}06 \pm 0{\cdot}06$ Mg/m^3, corresponding to a void ratio $e = 0{\cdot}30 \pm 0{\cdot}07$. The pellets were stored in the laboratory in a hermetic plastic box at 20°C. The initial suction ($s = 135 \pm 3$ MPa) was measured in the laboratory with a chilled mirror dew-point tensiometer (Decagon WP4C), corresponding to an initial water content $w = 7{\cdot}25\%$, slightly higher than the fabrication value, owing to further hydration after fabrication. Fig. 2 shows a photograph of a 7·14 mm high and 7·27 mm dia. pellet. It has a quasi-cylindrical shape with two spherical poles on the top and bottom.

Experimental methods

The determination of the water-retention properties under free swelling conditions was carried out by measuring the water content of pellets under suction controlled by vapour equilibrium, by placing the pellets in desiccators under saturated saline conditions. The changes in water content of the pellets were made by placing the pellet in desiccators containing either distilled water (for the wetting path) or a saturated saline solution (Table 1, for the drying path). The sample was periodically taken out of the desiccator to measure suction and weight.

The water content of the pellets was determined by oven-drying at 105°C for a period of 24 h. The specimen's volume was determined by hydrostatic weighing of waxed specimens into water (see Wan *et al*., 2013). The void ratio, degree of saturation, dry density and volumetric deformation of the samples were calculated from their volume, mass and water content.

The pore size distribution (PSD) curve were obtained on freeze-dried samples using an Autopore IV 9500 mercury intrusion porosimeter (Micromeritics) that operates at a maximum pressure of 230 MPa, corresponding to a minimum entrance diameter of 5·4 nm. Instantaneous freezing was

Table 1. Saline solutions used for suction control for the vapour equilibrium technique

Solution	Relative humidity at 20°C: %	Suction: MPa
Lithium chloride (LiCl)	15	261·5
Potassium carbonate (K_2CO_3)	44	113·2
Magnesium nitrate ($Mg(NO_3)_2$)	55	82·4
Sodium chloride (NaCl)	76	37·8
Ammonium sulfate ($(NH_4)_2SO_4$)	83·5	24·9
Potassium nitrate (KNO_3)	93·7	9

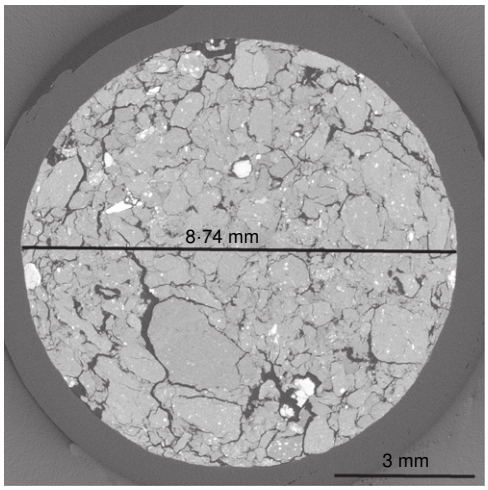

Fig. 3. Vertical section of a waxed pellet of bentonite at 1 MPa of suction

carried out by plunging the pellet into slushy nitrogen (−210°C) obtained by previously submitting it to vacuum (Delage *et al*., 2006). In such conditions, there is no nitrogen boiling around the samples when they are plunged into the nitrogen, resulting in quick freezing and good microstructure preservation with no ice expansion. In a standard fashion, the pore size distribution was interpreted assuming parallel, cylindrical non-intersecting pores.

The microstructure investigation was completed by X-ray μCT observations. The X-ray source's parameters were 80 kV and 40 μA. Voxel size was 4·41 μm. The samples were scanned using 1440 projections equally spread over 360°. After the reconstruction, 1298 horizontal slices were calculated (16-bit images; 1644 × 1292 pixels).

The reliability of the method of hydrostatic weighing of the waxed specimens to determine their volume was checked by using μCT so as to make sure that no wax infiltrated the swollen specimens presenting cracks. Fig. 3 shows a vertical slice of a waxed pellet of bentonite after hydration and swelling under a suction of 1 MPa, revealing the presence of significant cracks in the swollen bentonite. It can be observed that there are no gaps between the pellet and the wax and no infiltration of wax into the cracks connected to the sample surface, showing the validity of the method.

Test programme

The first series of suction-controlled tests (group A, Table 2, P0–P11) was aimed at determining the wetting (points P0 to P9) and drying (points P10 and P11) paths, starting from initial state P0 ($s = 135 \pm 3$ MPa, $w = 7{\cdot}25\%$, $\rho_d = 2{\cdot}06 \pm 0{\cdot}06$ Mg/m^3). The pellet that underwent wetting under 0 MPa (P9) did not reach the imposed suction after 20 d, with a suction of 0·8 MPa measured using the Decagon WP4 chilled mirror tensiometer.

Table 2. Testing programme

Sample		Path (imposed suction in MPa)		At equilibrium	
		I	II	Water content: %	Degree of saturation
A	P0	Initial state			
		135·5		6–7·25	54·5–66·1
	P1	113		7·9	53·5
	P2	82		9·4	63·4
	P3	40		15·6	63·1
	P4	38		16	64·1
	P5	25		16	60·7
	P6	9		24·6	63
	P7	4·2		31	63
	P8	1		43·5	61
	P9	0·8		45·4	71·8
	P10	149		6·3	45·2
	P11	262		3	25·9
B	P12	2·3	4·2	34·5	55·3
	P13	2·3	9	27·7	56·5
	P14	2·3	38	18·3	57·2
	P15	2·3	82·4	16·04	61·4
	P16	2·3	113	10·5	65·1
	P17	2·3	262	5·96	46·3

In the second series of tests (group B, Table 2, P12 to P17), the pellets were first hydrated by submitting them during 12 d to a 100% relative humidity in a desiccator containing distilled water (path I). WP4 suction measurements showed that they reached a suction of 2·3 MPa. The pellets were then dried (path II) to various suctions between 4·2 (P12) and 262 MPa (P17).

The water content and dry density of the samples of groups A and B were determined at equilibrium. MIP tests were performed on the specimens of group A (P0, P1, P2, P3, P4, P5, P6, P7, P8, P9, P10 and P11). In addition, X-ray observations were performed on specimens P0 (initial state, $s = 135{\cdot}5$ MPa), P6 ($s = 9$ MPa), P4 ($s = 38$ MPa) and P8 ($s = 1$ MPa).

EXPERIMENTAL RESULTS

Water-retention behaviour

The changes in water content over time along path I are shown in Fig. 4 for group A. The data show that, in most cases, equilibrium was achieved after 10 d except for sample P9 at zero suction.

For group B, an equilibrated water content of $35 \pm 2\%$ was reached after 12 d of hydration. Fig. 5, which presents the subsequent changes in water content along drying path II, shows that the drying phase is significantly faster than the wetting one, with specimen mass stabilisation observed at all suctions after 2 d, compared to the 10 d long periods observed along wetting paths.

The water-retention curve expressed in terms of water content plotted against suction is shown in Fig. 6 for the points from controlled suctions. Given that the points correspond to different pellets, some dispersion is observed, particularly between the points at 40 and 39 MPa (which are satisfactorily close) and that at 25 MPa, with almost the same water content of 16% (whereas it should be larger). Some dispersion is also observed around the initial state. The wettest points at 0·8 and 1 MPa are in good correspondence

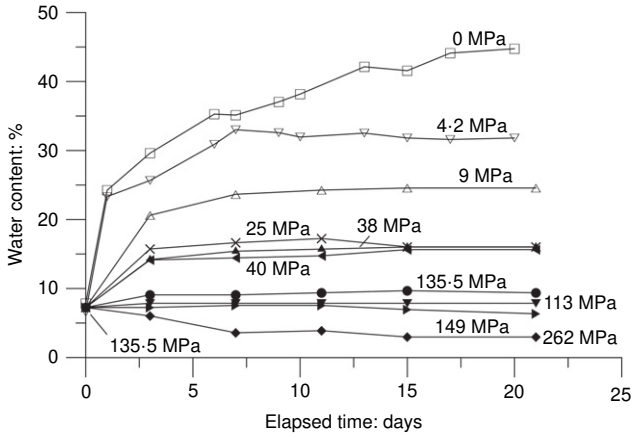

Fig. 4. Water content plotted against elapsed time during path I for group A

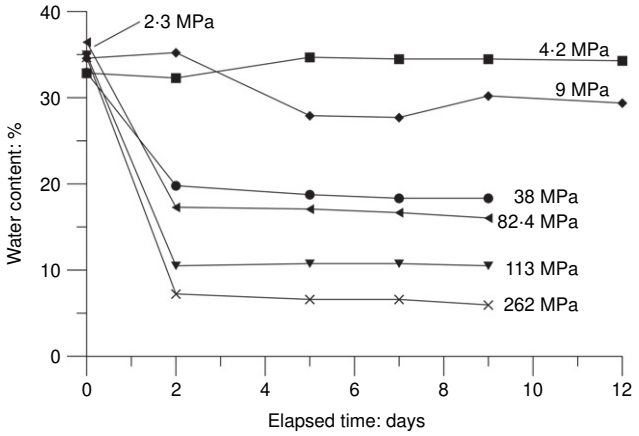

Fig. 5. Water content plotted against elapsed time during path II for group B

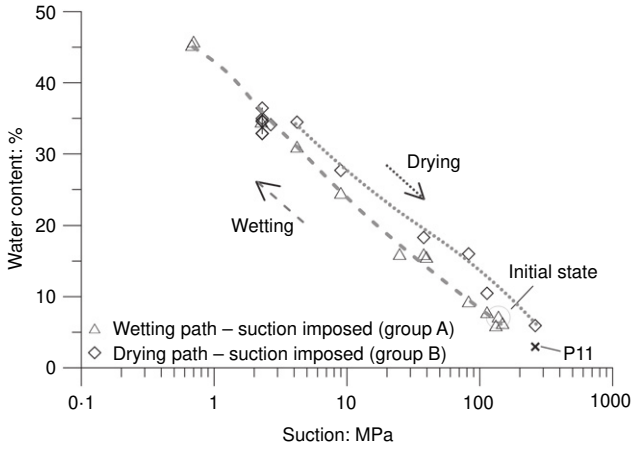

Fig. 6. Water content plotted against suction for all the specimens

with a maximum water content of 45·4%. Again, along the wetting path, the point at 4·2 MPa has a water content of 31% close to that at 2·3 MPa. It is, however, possible to draw averages curves to represent both the wetting and drying paths, with a slight hysteresis, including at the highest suction (262 MPa), where the point dried from the wetted state ($w = 6{\cdot}0\%$) is above that from the initial state ($w = 3{\cdot}0\%$). The hysteresis does not reduce at high suction, because of the dispersion between the various pellets tested.

The results obtained by the suction-controlled method are shown in Fig. 7 in terms of: (*a*) degree of saturation plotted against water content (Fig. 7(a)) and suction (Fig. 7(b)); (*b*) void ratio plotted against water content (Fig. 7(c)) and suction (Fig. 7(d)); and (*c*) volumetric strain plotted against water content (Fig. 7(e)) and suction (Fig. 7(f)). Fig. 7(b) shows that, for the points of group A along the wetting path, the degree of saturation increased from 55·3% to 60% when decreasing suction from 135·5 MPa (initial state) to 82 MPa; it stabilised afterwards at approximately 60% at lower suctions This feature, also described by Gatabin *et al.* (2016), reflects that swelling (see Fig. 7(e)) compensates for the increase in water content, keeping constant the ratio V_w/V_p (in which V_w is the volume of water and V_p is the total pore volume). This trend is confirmed by the linear shape of the *e*–*w* curve observed in Fig. 7(c), given that the void ratio $e = V_p/V_s$ (with V_s, the volume of the solid phase, constant) is proportional to V_p and w is proportional to V_w.

The changes in void ratio and in volumetric strain with respect to water content (Figs 7(c) and 7(e)) and suction (Figs 7(d) and 7(f)) confirm the significant swelling of the pellet at low suction: 120% swelling at 0·8 MPa suction, with a water content increase from 7·3 to 45·4%.

The points previously wetted to 2·3 MPa (group B, path II) stabilise at a smaller degree of saturation (around 56%) when suction is increased from 4·2 to 39 MPa. The degree of saturation increases afterwards to a maximum value of 65·1% at 113 MPa, prior to decreasing to 46·3% once dried at 262 MPa. Observation of Fig. 7(d) shows a monotonic decrease in water content with increased suction, except for the point at 113 MPa that exhibits a void ratio smaller than expected, explaining the peak in degree of saturation.

Microstructure changes during hydration

Mercury intrusion porosimetry. The results of MIP tests on samples P0-1 and P0-2 (initial state, 135 MPa suction), P10 (dried at 149 MPa suction) and P11 (dried at 262 MPa suction) are presented in Fig. 8. Tests P0-1 and P0-2, made in order to investigate repeatability issues and possible differences between pellets, provide similar PSD curves, illustrating good repeatability and comparable pellets. In all cases, a difference between the maximum void ratio intruded by mercury and the total void ratio of the pellets is observed in the cumulative curves (Fig. 8(a)). The total porosities of all pellets are similar except for P10 ($s = 149$ MPa), which has a slightly larger total porosity (0·39 compared to values around 0·34). In the case of heavily compacted smectite-bearing materials, the porosity that is not intruded at the highest mercury pressure (230 MPa), called here infra-porosity (Delage *et al.*, 2006), is related to small pores with entrance diameter smaller than 5·4 nm. The nature of these pores will be commented upon in more detail later on. The comparison of the curves shows that the various high suctions imposed here (135, 149 and 262 MPa) have no significant effect on the pore size distribution of the pellets, which are defined by a pore population with an average entrance diameter of 11·9 nm for samples at 135 MPa and 149 MPa and 10·7 nm for the pellet at 262 MPa. Cumulative and density functions curves also show a pore population at diameters around 4–5 μm that represents 6·8, 5·06 and 5·2% of the total porosity, for pellets at 135, 149 and 262 MPa respectively.

Figure 9 presents the pore size distribution curves of pellets hydrated from the initial state (135·5 MPa) to suctions higher than or equal to 25 MPa along the wetting paths: P1 (113 MPa), P2 (82 MPa), P3 (40 MPa), P4 (38 MPa) and P5 (25 MPa). The curves show that the average entrance pore radius remains 10·7 nm at 113 MPa, whereas it increases up

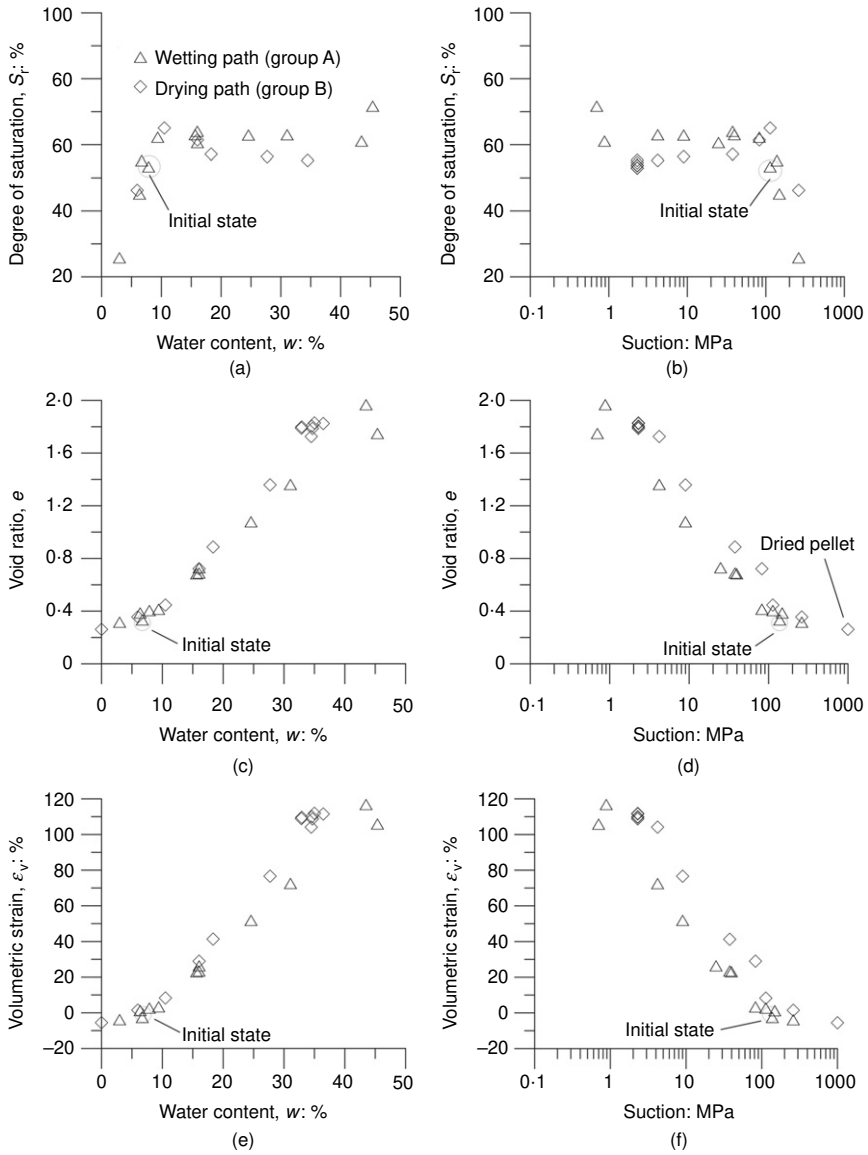

Fig. 7. Volumetric behaviour obtained by suction-controlled method: (a) degree of saturation plotted against water content; (b) degree of saturation plotted against suction; (c) void ratio plotted against water content; (d) void ratio plotted against suction; (e) volumetric strain plotted against water content; (f) volumetric strain plotted against suction

to 14·9 and 16·6 nm for suctions equal to or smaller than 82 MPa. Also, the pore population around 4–5 μm, previously observed at large suctions, is still observed at suctions of 113 and 82 MPa with comparable percentage of the total porosity (7·0% and 10·9%, respectively).

At lower suctions (40 MPa and below), the average diameter of large pores significantly increases to 30–40 μm, corresponding to a proportion of the total porosity of 8·3% for the pellets at 40 MPa.

To summarise, two kinds of cumulative curves are observed, showing no significant swelling between the initial state and states at suction larger than 82 MPa, whereas swelling due to the developments of pores in the range 10–40 μm is observed between 82 and 25 MPa.

Figure 10 presents the pore size distribution curves of pellets submitted to suctions equal to or lower than 25 MPa along the wetting path (P5 at 25 MPa, P6 at 9 MPa, P7 at 4·2 MPa, P8 at 1 MPa and P9 at 0·8 MPa). Whereas cumulative curves at 25 and 9 MPa remain comparable to that of the former series, the curve at 4·2 MPa looks like a transition towards the curves at lower suction, with a decrease in the peak previously observed at 19 nm and the development of pores with diameters up to 400 nm. At very low suction (1 and 0·8 MPa), no significant porosity is observed below 100 nm. The significant swelling is due to the development of pores with average diameters of 290 nm (suction 1 MPa) and 400 μm (suction 0·8 MPa), corresponding to 42·3% and 56·6% of the total porosity, respectively.

X-ray computed microtomography. X-ray μCT data are presented in Figs 11 and 12. Fig. 11 shows two horizontal sections (I, II) of pellet P0 at initial state (unit weight of 2·12 Mg/m^3 and suction 135 MPa) together with that of pellet P4 equilibrated under a suction of 38 MPa, with a smaller unit weight 1·64 Mg/m^3 due to swelling (also illustrated by the changes in diameter from 7·27 to 7·44 mm, and in height from 7·14 to 8·15 mm). Fig. 12 presents two horizontal sections of pellet P6 at 9 MPa suction (1·33 Mg/m^3) together with that of pellet P8 at 1 MPa suction (unit weight 0·93 Mg/m^3). The changes in diameter (7·92 mm at 9 MPa and 8·74 mm at 1 MPa from 7·27 mm at the initial state) and height (9·29 mm at 9 MPa and 10·54 mm at 1 MPa from 7·14 mm) of the pellets are also indicated.

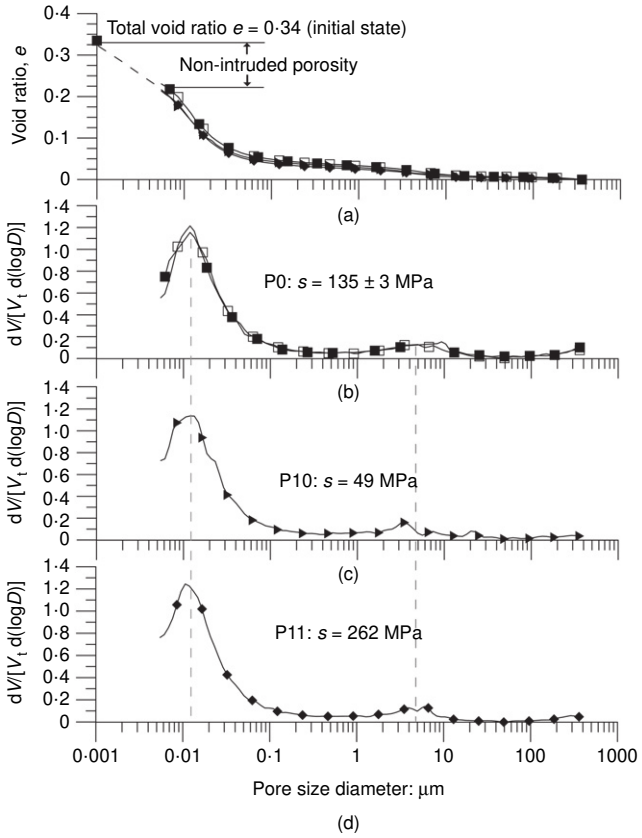

Fig. 8. MIP test results for P0, P10 and P11

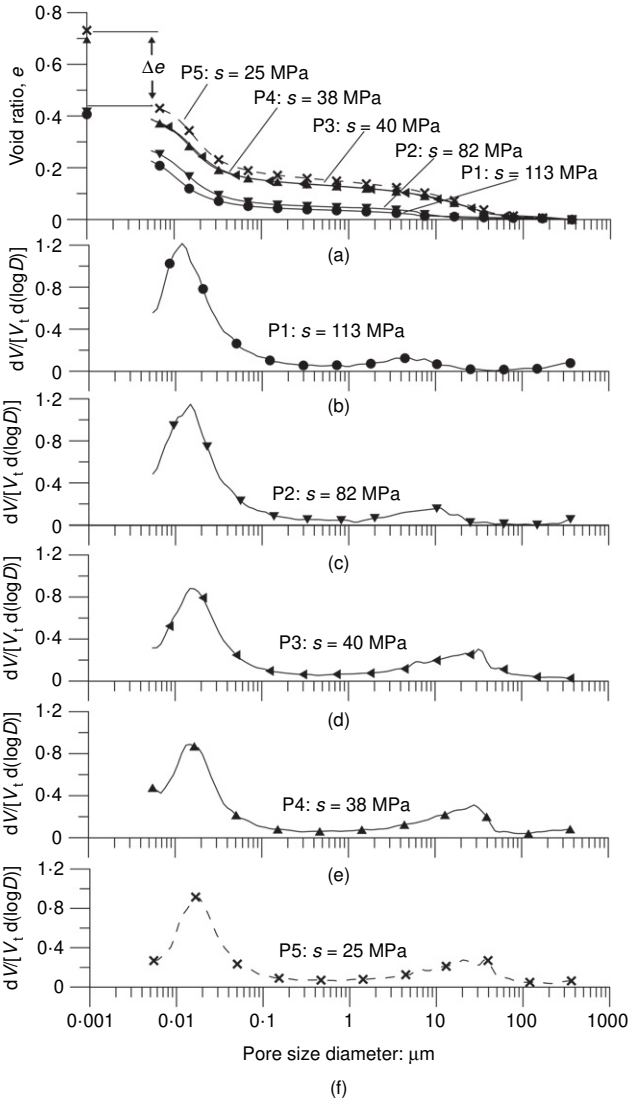

Fig. 9. MIP test results for P1–P5

Figure 13 compares the results of the volumetric strains obtained by hydrostatic weighing with wax to that calculated with the radial and axial strains. A good agreement is obtained for pellets at 9 and 38 MPa. However, at 1 MPa suction, the volumetric strain obtained by hydrostatic weighing is higher than that calculated from strains. This difference could be due to the fact that, unlike for samples at higher suctions, the two volume measurements at 1 MPa suction (hydrostatic weighing and size measurement) were not made on the same specimen.

A significant anisotropy in swelling is observed from size measurements, with axial swelling ε_a significantly larger than radial swelling ε_r, with a ratio $\varepsilon_a/\varepsilon_r$ of 6·1 at 38 MPa, 3·4 at 9 MPa and 2·4 at 1 MPa. This anisotropic response is linked to the fabrication process of a pellet, in which bentonite powder grains are instantaneously compacted in a mould in one-dimensional conditions, by increasing the axial stress, with no radial strain allowed. This results in an oriented structure with preferential sub-horizontal orientation of the particles that enhance swelling perpendicular to the smectite platelets.

Inspection of the sections of pellet P0 at initial state (Fig. 11, $s = 135$ MPa) shows, in upper section I, some cracks located close to the perimeter of the pellet, with an average thickness of 25·5 μm. These cracks are no longer visible in the middle section II. Cracks are also observed in pellet P4 hydrated at 38 MPa. They are also more apparent in section I compared to middle section II. Compared to the initial state, more cracks are observed in the middle section at 38 MPa.

For pellet P6 hydrated at 9 MPa suction (Fig. 12), the same phenomenon is observed, with more apparent cracks in the upper section I (average thickness of cracks 110 μm). Cracks observed in the middle section II result from the swelling and separation of bentonite grains (see the two grains with their dimensions marked in Fig. 12(a)).

Within the crack network, the grey levels of the continuous areas of compacted bentonite are comparable, providing evidence of reasonably constant density. However, this grey level cannot be directly related to the density of the pellet. Note that white sections correspond to crystals of higher density (calcite, quartz or pyrite, see Molinero-Guerra *et al.* (2016) for more details).

Sections of pellet P8, hydrated at 1 MPa of suction, clearly reveal apparent cracks on both sections (I and II). Some cracks inside bentonite grains are also observed (see the highlighted grain in section I in Fig. 12(b)). The deformability of the pellet is also evidenced in section I, where a change of the initial circular section is observed.

Three-dimensional reconstructions of pellets at initial state, and hydrated at 38, 9 and 1 MPa, as well as the crack network of a region of interest taken in the centre of the pellets, are presented in Fig. 14, providing a global view of the global changes of the pellets, as well as in their vertical sections. Compared to the photo at initial state (Fig. 14(a), described in detail in the paper by Molinero-Guerra *et al.* (2016)), which exhibits a rather homogeneous and compact mass with only some cracks at the top, the hydration at 38 MPa (Fig. 14(b)) provides evidence of the development of some disconnected cracks around and inside the pellet, particularly at the top. The aperture of the cracks has been determined based on the number of pixels contained in it.

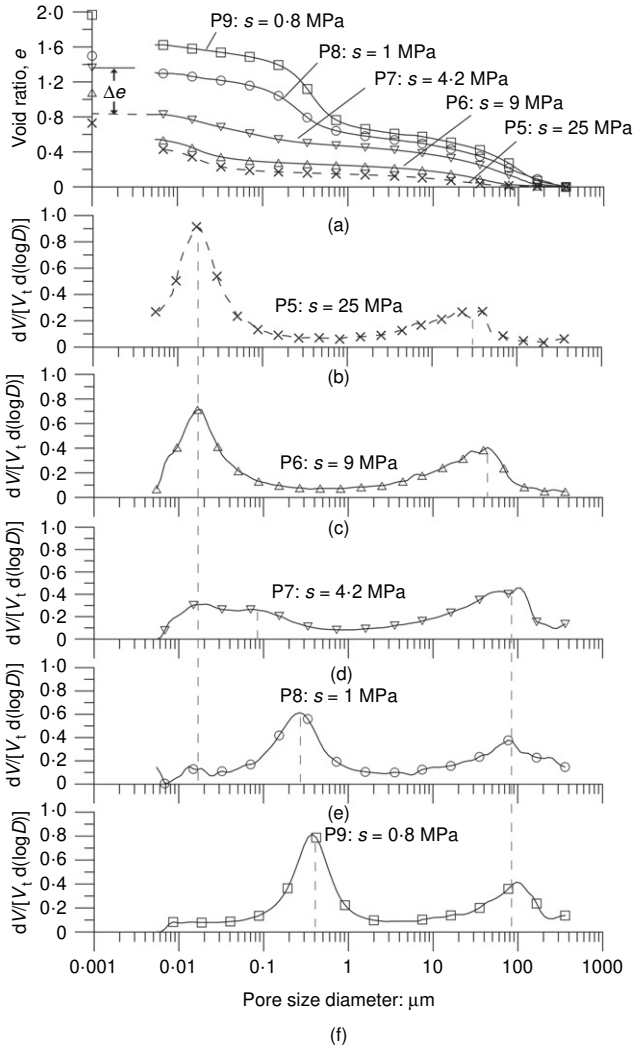

Fig. 10. MIP test results for P5–P9

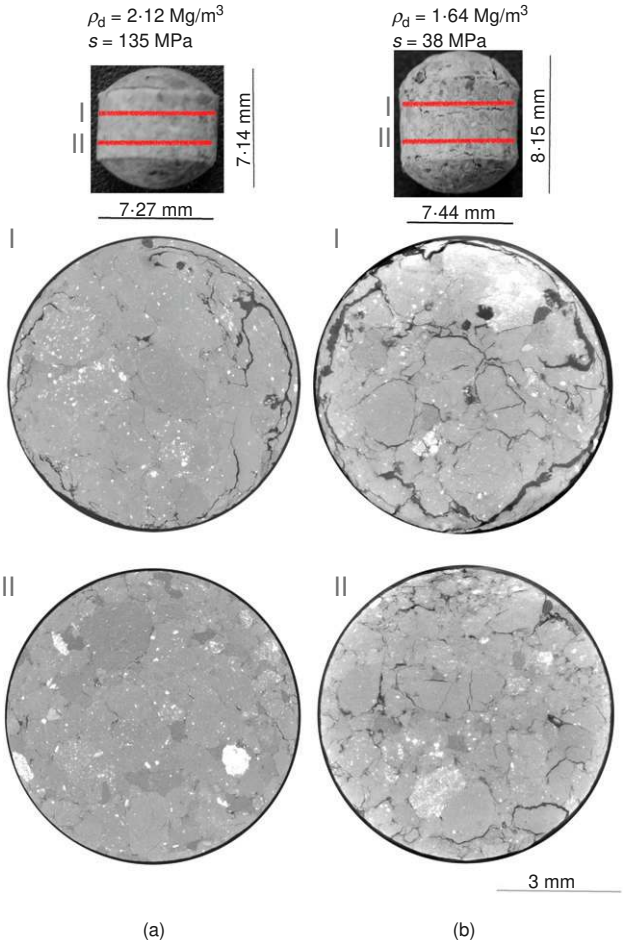

Fig. 11. X-ray μCT observations – horizontal section: (a) 135 MPa (P0); (b) 38 MPa (P4)

That of the external cracks is between 76·8 and 122·4 μm at the top, and between 37·9 and 84·8 μm close to the bottom.

As observed in the sections of Fig. 14(c), the aspect of the pellet hydrated and swelled under 9 MPa suction (volumetric swelling of 55·8%) is quite different, showing that swelling is due in significant part to the development of an interconnected crack network, further evidenced by the 3D reconstruction of cracks. As commented above, the bentonite pieces within the crack network have comparable density. Their average size is between 44·2 μm and 246·4 μm. The appearance of the solid phase of the pellet under 1 MPa (volumetric swelling of 88·1%, Fig. 14(d)) is not that different from that under 9 MPa; the difference is more apparent in the crack network, with more cracks and more interconnection between them. The average size of the cracks is between 171 μm and 487 μm.

An attempt was made to run X-ray μCT observations on a sample hydrated at 0·8 MPa; but the sample, close to full hydration, became weak and soft, not far from a slurry, and it was not possible to handle it safely to perform the test.

DISCUSSION

X-ray μCT provides some complementary information at larger scale on the pellet microstructure, with respect to MIP data. The observation at initial state (suction of 135 MPa) provides evidence of some circular cracks close to the edge, on the top section of the pellet, which are likely to be a consequence of stress release after the pellet manufacturing by rapid compacting. These cracks apparently play a role during the release of suction down to 38 MPa, with an enlargement of the circular cracks on the top section, and some development of internal cracks. Obviously, cracks favour the penetration of water vapour within the pellets. Internal cracks are more frequent at lower suctions (9 and 1 MPa); they develop between bentonite grains, which are sometimes affected by internal cracks. The swelling of the pellet is hence due to the combined action of crack propagation (better observed by using X-ray μCT) and the expansion of bentonite grains (quantified by MIP).

Referring to the PSD curves of Figs 8–10, X-ray μCT data indicate that the large pore populations observed in MIP above 10 μm correspond to cracks. MIP curves confirm that the crack network is not very developed at initial state (135 MPa), at which MIP data indicate that 6·8% of the total porosity has access diameters between 2 and 10 μm. This pore population is observed in the 3D crack reconstruction of Fig. 14(a).

As seen in the PSD curves, a distinction can be made between the curves at initial state, 113 and 82 MPa, with those at 40 and 25 MPa with respect to the development of the large pores between 4 and 100 μm observed in the curves at 40 and 25 MPa. As indicated by X-ray μCT, this is related to the development of the more apparent cracks network observed in Figs 14(b)–14(d). Based on the 3D reconstruction of both the pellet and the crack network (centre and

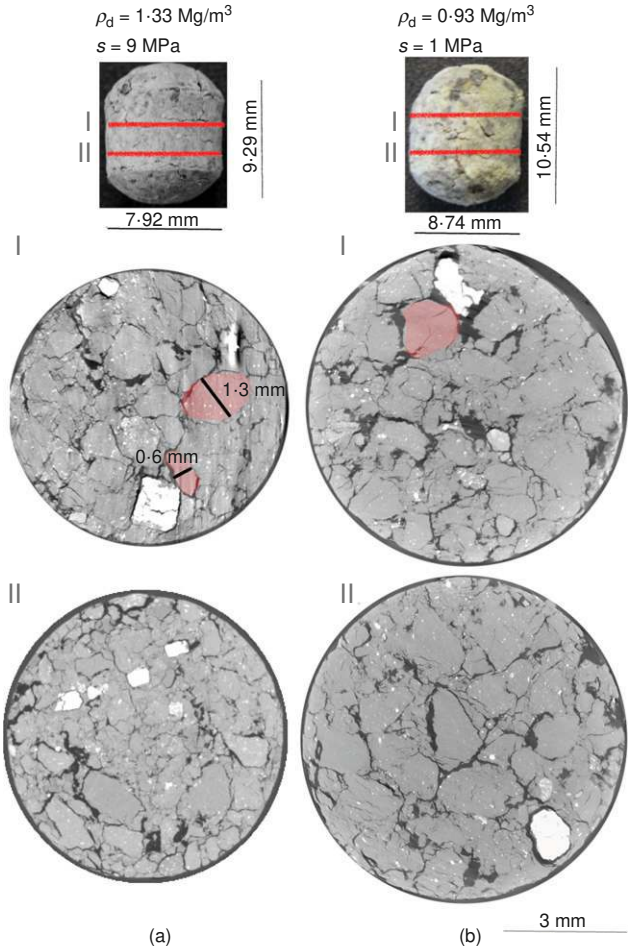

Fig. 12. X-ray μCT observations – horizontal section: (a) 9 MPa (P6); (b) 1 MPa (P8). A full-colour version of this figure can be found on the ICE Virtual Library (www.icevirtuallibrary.com)

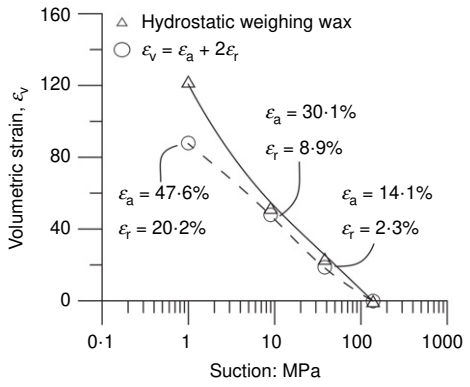

Fig. 13. Volumetric strain (ε_v) obtained by hydrostatic weighing wax compared to that calculated with the radial (ε_r) and axial (ε_a) strain

right-hand side images), it seems that the interconnection between cracks is more apparent at 9 MPa compared to 25 MPa, whereas the difference in PSD between 25 and 9 MPa is not straightforward, apart from the shift of the peak in density function from 30 to 40 μm (Figs 10(b) and 10(c)). At lower suctions (4·2, 1 and 0·8 MPa), the peak shifts toward 80 μm (Figs 10(d)–10(f)), linked with the increase in the interconnection of cracks observed at 1 MPa suction in the X-ray μCT data of Fig. 14(d).

The changes in PSD curves in the small pore range are governed by different phenomena at a different scale, with average pore diameters of 11 nm at initial state and at a suction of 262 MPa. Applying higher suctions along the drying path has no effect on this pore population, as also observed in the decrease from 135 to 113 MPa suction. The measured intruded porosity is the same (0·22) at suctions between 262 and 113 MPa (see Fig. 8), and it slightly increases at 0·26 at 82 MPa, prior to reaching 0·38 at 40 MPa (Fig. 9).

These features can be interpreted based on findings on the hydration mechanisms of smectites, that come from investigations on pure smectites (e.g. Mooney *et al.*, 1952; Méring & Glaeser, 1954; Norrish, 1954) and have been extended to compacted smectite (Saiyouri *et al.*, 2000, 2004, Delage, 2007). As recalled in Fig. 15, the inter-basal spacing of smectites, illites and interlayer illite–smectite minerals (all minerals made up of an octahedral layer between two tetrahedral layers) is equal to 0·96 nm. During hydration, the inter-basal spacing of smectites is known to increase in an orderly fashion due to the successive adsorption of layers of water molecules. X-ray diffraction techniques demonstrated that, during hydration, the successive adsorption of one, two or three layers of water molecules along the smectite minerals corresponded to interlayer spacing of 1·26, 1·56 and 1·86 nm, respectively (corresponding to an equivalent thickness of 0·3 nm for an individual layer of water molecules). Another important result (see e.g. Ben Rhaïem *et al.*, 1987; Cases *et al.*, 1992; Bérend *et al.*, 1995; Saiyouri *et al.*, 2004; Ferrage *et al.*, 2005, 2007) is that the number of layers adsorbed depends on the relative humidity (or suction) imposed during hydration. As an example, Saiyouri *et al.* (2004) observed, in a compacted MX 80 Wyoming montmorillonite specimen, that one layer of water molecules was adsorbed at suctions larger than 50 MPa, two layers between 50 and 7 MPa, and three layers below 7 MPa, with a fourth layer adsorbed at low suctions smaller than 0·1 MPa. This mechanism is illustrated in Fig. 15. Saiyouri *et al.* (2004) also observed during hydration a constant decrease in thickness of the smectites platelets starting from stacks made up of around 300 layers down do around ten layers at suctions smaller than 9 MPa. Actually, in addition it was shown that this reduction in platelets' thickness at low suction also corresponded to a larger disorder of the microstructure of the compacted bentonite due to the exfoliation of the aggregates.

In this framework, it seems convenient to analyse PSD curves by using the simplified brick model that consists in considering that the well-organised pore diameter distribution around an average diameter observed at suctions larger than 9 MPa provides an estimation of the average thickness of the clay platelets. The data of Fig. 15 indicate that, with one layer adsorbed at large suctions of various hundreds of MPa, the thickness of the smectite layer is equal to 1·26 nm, providing an average thickness of the platelet of 11 nm, corresponding to a number of nine layers per platelets.

The diagram in Fig. 15 indicates an increase from one to two layers adsorbed when suction is decreased below 50 MPa. With two layers of water molecules, providing an inter-basal spacing of 1·56 nm at 40 MPa, a thickness of 14 nm can be calculated at suctions between 50 and 7 MPa. This value is reasonably comparable with the value of 14·9–16·6 nm obtained from the PSD curve by using the brick model for suctions between 40 and 9 MPa.

The combined use of MIP and X-ray μCT investigations, alongside an interpretation based on the hydration mechanisms of smectites, hence helps in better understanding the changes in microstructure of a bentonite pellet subjected to change in suction through the vapour phase. It confirms that the development of cracks contributes in a significant

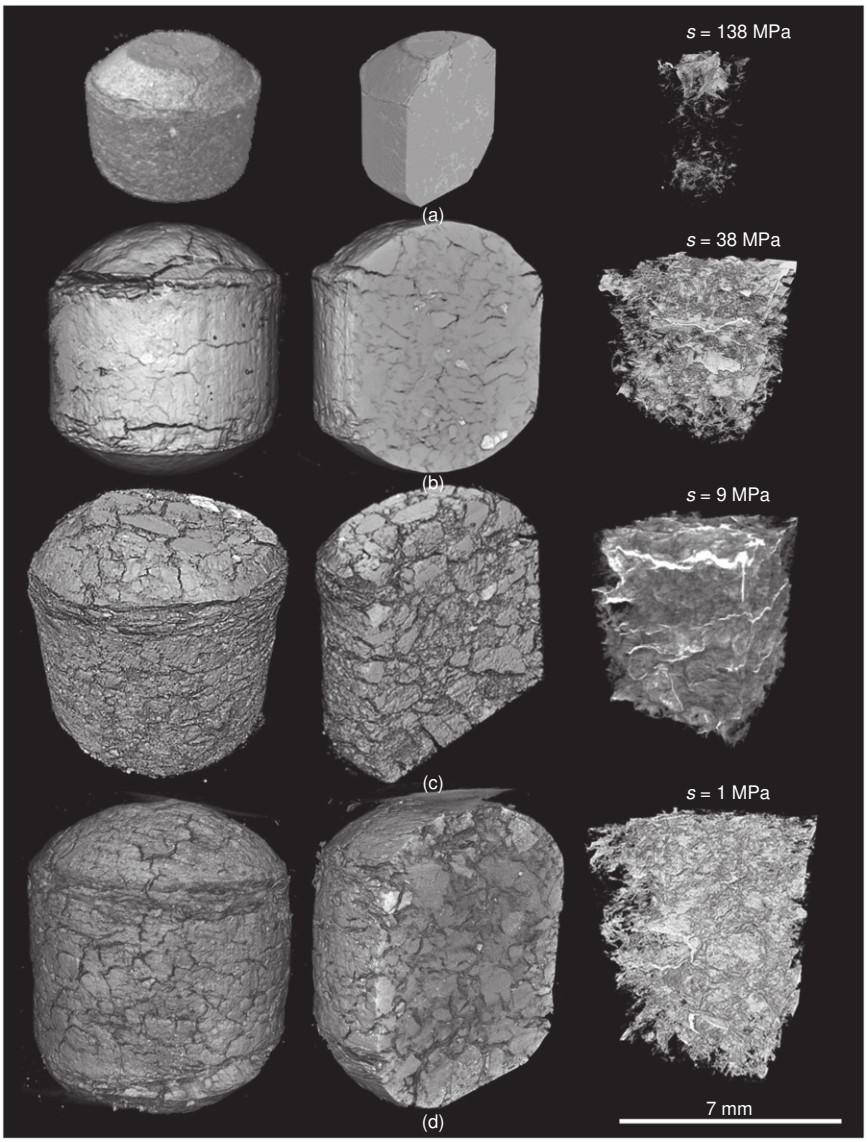

Fig. 14. X-ray μCT observations – 3D reconstruction image and network of cracks: (a) P0 – initial state; (b) P4 – $s = 38$ MPa; (c) P6 – $s = 9$ MPa; (d) P8 – $s = 1$ MPa

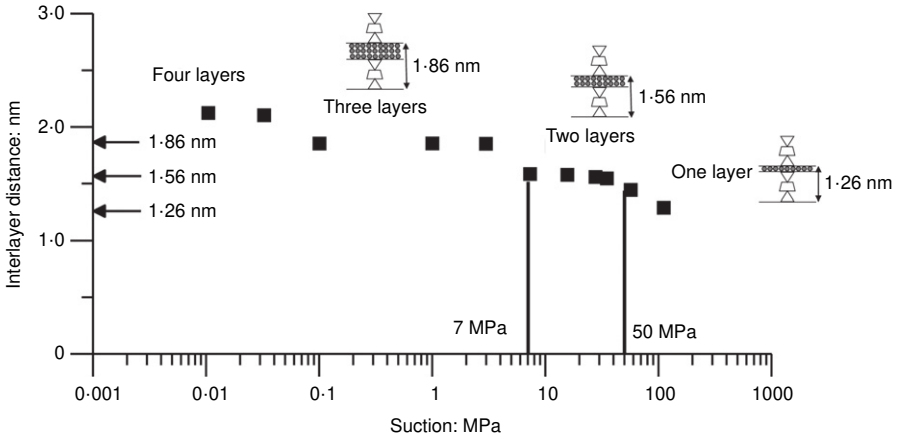

Fig. 15. Interlayer distance plotted against suction pressure for smectites (after Saiyouri *et al.*, 2004)

manner to the swelling of the pellet, whereas 1, 2 and 3W adsorption mechanisms along the smectite mineral at the nanometre level are relevant to identify the simultaneous intra-platelet swelling mechanism.

CONCLUSION

To understand better the water-retention properties of pellets of MX80 bentonite used as engineered barriers and plugs in some concepts for radioactive waste disposal at great

depth, the change in microstructure of a pellet subjected to suction changes was investigated at small scale by means of MIP tests on freeze-dried specimens, complemented at larger scale by X-ray μCT observations carried out on intact specimens.

Along the drying path at suctions larger than the initial one (135 MPa), MIP does not provide evidence of any significant change in PSD, and it is likely that cracks, which are not very apparent at 135 MPa, do not develop further. The tiny changes observed in microstructure are linked to the mechanisms of water adsorption at the nano scale along the smectite faces, which are governed, at suctions of several hundreds of MPa, by 1W adsorption and a constant inter-basal distance of 1·26 nm. The average entrance pore radius at initial and drier states is related to the average thickness of the 1W hydrated smectite platelets, with no evidence of inter-aggregate pores of larger size. This suggests that the powder grains are very closely packed together within pellets, as already observed by Molinero-Guerra *et al*. (2016).

Along the wetting path, swelling is due to the combined effect of crack propagation at the macro scale, and the swelling of bentonite grains, which is governed by the hydration mechanisms of smectite at the nano scale, with 2W hydration at suctions between 82 and 9 MPa. In this suction range, the changes in average entrance diameter are not very significant in MIP, and both MIP and X-ray μCT provide evidence of the role played by crack propagation in swelling, with significant development of a crack network between 38 and 9 MPa. The application of suctions below 9 MPa is known to result in 3W hydration in smectites, corresponding to a significant decrease of the platelet thickness and to an increase in the disorder of the platelet assembly (Saiyouri *et al*., 2004). At low suction, hydrated smectites are known to be made up of thin platelets of around ten layers (Tessier, 1990; Saiyouri *et al*., 2004), with open card house structures that may explain the large entrance diameter observed in the MIP investigation conducted in this work, which evidenced an increase in average entrance pore radius up to 0·4 μm within the expanded bentonite grains. Both X-ray μCT and MIP also indicate that the crack network develops significantly.

Cracks are hence suspected to play an important role in the propagation of water vapour into the pellets during hydration and swelling. Given that the in situ hydration of pellets in deep radio-active disposal in claystones will occur at the contact between some pellets and the low-permeability host rock through a very small flux of liquid water, vapour transfers through the inter-pellets porosity might play a significant role, at least at the beginning of the hydration phase. The investigations carried out in this work showed that the hydration of an individual pellet under free swelling conditions occurred within a period of time of 20–30 d, which provides an idea of the timescale involved, at least in ideal conditions. Of course, free swelling conditions will only hold as long as all the inter-pellets porosity is not filled by the expansion of deformable hydrating pellets. Once the continuity of the vapour phase has stopped, it is likely that liquid hydration will become more significant and will govern the hydration kinetics.

It seems that the hydration mechanism of the mass of pellets should be investigated in more detail by numerically modelling vapour phase transfers and the transition towards liquid water transfers. In this regard, the hydration boundary conditions at the interface between the pellets and the host rock require further attention, together with the effects of the development of cracks and their subsequent closure after swelling.

ACKNOWLEDGEMENTS

This work is part of the PhD thesis of the first author, carried out at Ecole des ponts ParisTech with the financial and scientific support of the IRSN (Institut de radioprotection et de sûreté nucléaire), the French public service expert in nuclear and radiation risks.

REFERENCES

Agus, S. S. & Schanz, T. (2005). Effect of shrinking and swelling on microstructures and fabric of a compacted bentonite–sand mixture. In *Proceedings of the international conference on problematic soils* (eds H. Bilsel and Z. Nalbantoglu), vol. 2, pp. 543–550. Famagusta, North Cyprus: Eastern Mediterranean University Press.

Alonso, E. E., Romero, E., Hoffmann, C. & Garcia-Escudero, E. (2005). Expansive bentonite–sand mixtures in cyclic controlled-suction drying and wetting. *Engng Geol.* **81**, No. 3, 213–226.

Ben Rhaïem, H., Pons, C. H. & Tessier, D. (1987). Factors affecting the microstructure of smectites. Role of cation and history of applied stresses. In *Proceedings of the international clay conference*, Denver, CO, USA (eds L. G. Schultz, H. Van Olphen and F. A. Mumpton), pp. 292–297. Bloomington, IN, USA: The Clay Minerals Society.

Bérend, I., Cases, J. M., François, M., Uriot, J. P., Michot, L., Masion, I. A. & Thomas, F. (1995). Mechanism of adsorption and desorption of water vapor by homoionic montmorillonites: 2. The Li+, Na+, K+, Rb+ and Cs+-exchanged forms. *Clay Clay Miner.* **43**, No. 3, 324–336.

Cases, J. M., Berend, I., Besson, G., Francois, M., Uriot, J. P., Thomas, F. & Poirier, J. E. (1992). Mechanism of adsorption and desorption of water vapor by homoionic montmorillonite. 1. The sodium-exchanged form. *Langmuir* **8**, No. 11, 2730–2739.

Cui, Y. J., Loiseau, C. & Delage, P. (2002). Microstructure changes of a confined swelling soil due to suction controlled hydration. In *Proceedings of the 3rd international conference on unsaturated soils* (eds J. F. T. Jucá, T. M. P. de Campo and F. A. M. Marinho), vol. 2, pp. 593–598. Rotterdam, the Netherlands: A. A. Balkema.

Delage, P. (2007). Microstructure features in the behaviour of engineered barriers for nuclear waste disposal. In *Experimental unsaturated soils mechanics: proceedings of international conference on mechanics of unsaturated soils* (ed. T. Schanz), pp. 11–32. Weimar, Germany: Springer.

Delage, P., Marcial, D., Cui, Y. J. & Ruiz, X. (2006). Ageing effects in a compacted bentonite: a microstructure approach. *Géotechnique* **56**, No. 5, 291–304, https://doi.org/10.1680/geot.2006.56.5.291.

Dixon, D. A., Gray, M. N. & Graham, J. (1996). Swelling and hydraulic properties of bentonites from Japan, Canada and the USA. *Environ. Geotech.* **1**, No. 1, 43–48.

Ferrage, E., Lanson, B., Sakharov, B. A. & Drits, V. A. (2005). Investigation of smectite hydration properties by modeling experimental X-ray diffraction patterns: Part I. Montmorillonite hydration properties. *Am. Miner.* **90**, No. 8–9, 1358–1374.

Ferrage, E., Kirk, C. A., Cressey, G. & Cuadros, J. (2007). Dehydration of Ca-montmorillonite at the crystal scale. Part 2. Mechanisms and kinetics. *Am. Miner.* **92**, No. 7, 1007–1017.

Gatabin, C., Talandier, J., Collin, F., Charlier, R. & Dieudonné, A. C. (2016). Competing effects of volume change and water uptake on the water retention behaviour of a compacted mx-80 bentonite/sand mixture. *Appl. Clay Sci.* **121–122**, 57–62.

Graham, J., Saadat, F., Gray, M. N., Dixon, D. A. & Zhang, Q. Y. (1989). Strength and volume change behaviour of a sand–bentonite mixture. *Can. Geotech. J.* **26**, No. 2, 292–305.

Hoffmann, C., Alonso, E. E. & Romero, E. (2007). Hydro-mechanical behaviour of bentonite pellet mixtures. *Phys. Chem. Earth* **32**, No. 8–14, 832–849.

Imbert, C. & Villar, M. V. (2006). Hydro-mechanical response of a bentonite pellets/powder mixture upon infiltration. *Appl. Clay Sci.* **32**, No. 3-4, 197–209.

Karnland, O., Nilsson, U., Weber, H. & Wersin, P. (2008). Sealing ability of Wyoming bentonite pellets foreseen as buffer material – Laboratory results. *Phys. Chem. Earth* **33**, No. Suppl. 1, 472–475.

Kawaragi, C., Yoneda, T., Sato, T. & Kaneko, K. (2009). Microstructure of saturated bentonites characterized by X-ray CT observations. *Engng Geol.* **106**, No. 1-2, 51–57.

Komine, H. & Ogata, N. (1994). Experimental study on swelling characteristics of compacted bentonite. *Can. Geotech. J.* **31**, No. 4, 478–490.

Kozaki, T., Suzuki, S., Kozai, N., Sato, S. & Ohashi, H. (2001). Observation of microstructures of compacted bentonite by microfocus X-ray computerized tomography (micro-CT). *J. Nucl. Sci. Technol.* **38**, No. 8, 697–699.

Méring, J. & Glaeser, R. (1954). Sur le rôle de la valence des cations échangeables dans la montmorillonite. *Bulletin de la Société Francaise de Minéralogie et Cristallographie* **77**, 519–530 (in French).

Molinero-Guerra, A., Mokni, N., Delage, P., Cui, Y. J., Tang, A. M., Aimedieu, P., Bernier, F. & Bornert, M. (2016). In-depth characterisation of a mixture composed of powder/pellets MX80 bentonite. *Appl. Clay Sci.* **135**, 538–546.

Montes, G., Duplay, J. & Martinez, L. (2001). Study of bentonite swelling : qualitative and quantitative analysis using ESEM and digital image analysis program. *Proceedings of 12th international clay conference*, Bahia Blanca, Argentina.

Mooney, R. W., Keenan, A. C. & Wood, L. A. (1952). Adsorption of water vapor by montmo-rillonite. II. Effect of exchangeable ions and lattice swelling as measured from X-ray diffraction. *J. Am. Chem. Soc.* **74**, 1371–1374.

Norrish, K. (1954). The swelling of montmorillonite. *Discussions Faraday Soc.* **18**, 120–134.

Pusch, R. (1982). Mineral–water interactions and their influence on the physical behavior of highly compacted Na bentonite. *Can. Geotech. J.* **19**, No. 3, 381–387, https://doi.org/10.1139/t82-041.

Saba, S. (2013). *Comportement hydromécanique différé des barrières ouvragées argileuses gonflantes*. PhD thesis, Ecole des Ponts ParisTech – Université de Paris Est, Marne-la-Vallée, France (in French).

Saba, S., Barnichon, J. D., Cui, Y. J., Tang, A. M. & Delage, P. (2014). Microstructure and anisotropic swelling behaviour of compacted bentonite/sand mixture. *J. Rock Mech. Geotech. Engng* **6**, No. 2, 126–132.

Saiyouri, N., Hicher, P. Y. & Tessier, D. (2000). Microstructural approach and transfer water modelling in highly compacted unsaturated swelling clays. *Mech. Cohesive Frictional Mater.* **5**, No. 1, 41–60.

Saiyouri, N., Tessier, D. & Hicher, P. Y. (2004). Experimental study of swelling in unsaturated compacted clays. *Clay Miner.* **39**, No. 4, 469–479.

Schuster, K., Furche, M., Velasco, M., Gaus, I., Trick, T., Garcia-Siñeriz, J. L., Rey, M., Schulte, F., Sanchez Herrero, S., Tietz, T. & Mayor, J. C. (2014). *Long-term performance of engineered barrier systems PEBS. Engineered barrier emplacement experiment in Opalinus Clay: "EB" experiment. Horizontal borehole results (geophysics, hydro test, laboratory tests)*. Brussels, Belgium: European Commission.

Seiphoori, A., Ferrari, A. & Laloui, L. (2014). Water retention behaviour and microstructural evolution of MX-80 bentonite during wetting and drying cycles. *Géotechnique* **64**, No. 9, 721–734, https://doi.org/10.1680/geot.14.P.017.

Sugita, Y., Chijimatsu, M. & Suzuki, H. (2005). Fundamental properties of bentonite pellet for prototype repository project. In *Advances in understanding engineered clay barriers* (eds E. E. Alonso and A. Ledesma), pp. 293–299. Leiden, the Netherlands: A. A. Balkema.

Sun, W., Sun, D., Fang, L. & Liu, S. (2014). Soil-water characteristics of Gaomiaozi bentonite by vapour equilibrium technique. *J. Rock Mech. Geotech. Engng* **6**, No. 1, 48–54.

Svemar, C. & Pusch, R. (2000). *Project description FIKW-CT-2000-00055*, Progress Report IPR-00-30. Solna, Sweden: SKB International.

Tessier, D. (1990). *Matériaux argileux: Structure, propriétés et applications* (ed. A. Decarreau), vol. 1, pp. 387–445. Paris, France: Société Française de Minéralogie et Cristallographie (in French).

Van Geet, M., Volckaert, G. & Roels, S. (2005). The use of microfocus X-ray computed tomography in characterising the hydration of a clay pellet/powder mixture. *Appl. Clay Sci.* **29**, No. 2, 73–87.

Wan, M., Delage, P., Tang, A. M. & Talandier, J. (2013). Water retention properties of the Callovo-Oxfordian claystone. *Int. J. Rock Mech. Min. Sci.* **64**, 96–104.

Wang, Q., Cui, Y. J., Tang, A. M., Barnichon, J. D., Saba, S. & Ye, W. M. (2013). Hydraulic conductivity and microstructure changes of compacted bentonite/sand mixture during hydration. *Engng Geol.* **164**, 67–76.

Wang, Q., Cui, Y. J., Tang, A. M., Li, X. L. & Ye, W. M. (2014). Time- and density-dependent microstructure features of compacted bentonite. *Soils Found.* **54**, No. 4, 657–666.